Solid Freeform Fabrication 2022: Proceedings of the 33rd Annual International Solid Freeform Fabrication Symposium – An Additive Manufacturing Conference
Reviewed Paper

Relationship between flow-controlled fiber orientation and spring-in deformation in extrusion deposition additive manufacturing

Akshay.J. Thomas*, Eduardo Barocio*, Vasudha Kapre*, Pasita Pibulchinda*, Felix N. Nguyen**, and R. Byron Pipes*

*Composites Manufacturing and Simulation Center - Purdue University. West Lafayette, IN, USA.
** Lockheed Martin Corporation

Abstract

Extrusion deposition additive manufacturing (EDAM) with fiber-filled polymers has enabled the printing of structures in the scale of multiple meters owing to enhanced stiffness and lower coefficient of thermal expansion primarily in the printing direction. Developing manufacturing process simulations for EDAM requires extensive material characterization including mechanical, thermal, viscoelastic, and thermomechanical property characterization. Further, varying the bead deposition conditions alter the fiber orientation state of the composite, thereby resulting in different anisotropic material properties. This increases the amount of characterization required to enable the digital twin framework. Therefore, we present a framework to infer the fiber orientation properties by conducting limited tensile tests at the composite coupon level. Using the inferred orientation state, we predict the unmeasured mechanical and thermomechanical properties and bypass the need for their experimental characterization. We present the application of this framework to predict the spring-in deformation of a geometry of interest printed using different process conditions.

Keywords: Fiber Orientation, Spring-in, Virtual Characterization

Introduction

Extrusion Deposition Additive Manufacturing is a process taht starts with pelletized fiber-filled polymers which are melted in an extruder and subsequently deposited on to a build platform in a layer-by-layer basis. The scalability of the EDAM process is successful due to the presence of fibers that enhance the elastic properties and decrease the coefficient of thermal expansions of the printed material, dominantly in the print direction [1], [2]. EDAM has, therefore, found applicability in printing geometries for autoclave tooling [3], [4] and compression molding [5]. The manufacturing process in EDAM involves multiple physics that develop concurrently, including anisotropic heat transfer, polymer crystallization and melting, stress relaxation, polymer shrinkage, and fusion bonding. The effects of this multi-physics phenomenon present themselves as residual stress and deformation in the printed part, that in turn cause delamination of the part. This has motivated the development of physics-based models to predict the outcome of the printing process [6]–[8]. Simulations have been successful in predicting and optimizing the yield stress of printed acrylonitrile–butadiene–styrene (ABS) [9], predict failure criteria in parts manufactured by selective laser sintering [10], and understand the effect of printing angle and layer thickness on the elastic properties of parts manufactured by fused deposition modeling (FDM) [11].

Choosing optimal printing conditions to build a part is a crucial step to minimize part deformation and residual stresses of the printed structure. Multiple printing parameters including the nozzle size, bead dimensions, printing speed, and extrusion temperature can be varied. The processing parameters induces different microstructures in the printed bead leading to varied elastic properties, viscoelastic behavior, thermo-elastic properties, and strength. Recently, Yan et.al. [12] showed that processing conditions critically effect the fiber orientation state in a printed bead. Their systematic experimental study is of immense importance as it brings to the reader's attention that the displacement and stress profile in a printed part could vary with processing conditions. Pibulchinda et.al. [13] conducted a virtual investigation of varying fiber orientation on deformation of a printed part by considering extreme cases of fiber orientation state. While physics-based manufacturing

simulations equip an engineer to understand the effect of processing conditions on the final deformation and stress state of a part, it often is accompanied by extensive characterization, including the mechanical, transport, and thermo-viscoelastic properties. These properties are dependent on the properties of the constituents (fiber and polymer), and the micro-structural characteristics of the printed bead such as the fiber length distributions, the fiber aspect ratio, and the orientation state of the fibers. The orientation state of the fibers is one of the most important microstructural aspects that govern the mechanical, transport, and thermoviscoelastic properties of the composite[14],[15],[16]. However, characterizing all the inputs needed for the process simulations experimentally is infeasible. Hence, micromechanics models have been used to augment experimental measurements. Micromechanics models require the constituent properties, and microstructure description to make predictions.

As the fiber orientation state is an important descriptor of the microstructure, simulation methods have been developed to predict them in injection and compression molding [17]. To the best of our knowledge such methods are underdeveloped in EDAM. Experimental methods including CT scans and optical microscopy can also be used to measure the fiber orientation. These methods, however, are prone to human error and are time consuming. Further, the spatial resolution of CT scans required to resolve single fibers is limited to volumes that are much smaller than the printed bead. Similarly, optical methods allow the fiber orientation resolution limited to cylindrical fibers or clusters of non-cylindrical fibers.

To understand the effects of processing conditions on the residual deformation of a geometry under these circumstances, much effort is required to populate the material card (material properties describing physical phenomenon). Further, as the study from Yan et.al [12] indicates, assuming the same material properties across different processing conditions would lead to erroneous interpretations. Therefore, the objective of this paper is to understand the effect flow-controlled fiber orientation developed during the bead deposition process on the mechanical properties and residual spring-in deformation in EDAM. We begin by conducting a design of experiments on certain bead deposition parameters. We next print panels to extract coupons for tensile testing. Following this step, we use an inference methodology to infer the fiber orientation state corresponding to the printing conditions that lead to the highest and lowest stiffness values. We then use this fiber orientation state to populate the mechanical, thermomechanical, transport, and viscoelastic properties. Finally, we use the generated material card to run manufacturing simulations of a part prone to spring-in deformation.

Experimental Methodology

We start by discussing the various processing conditions. Before the discussion on the experimental tests, we motivate the choice of the bead deposition conditions. The molten extrudate exits the nozzle, turns 90 degrees and gets compacted using a mechanical tamper as it is laid down on the heated substrate or previous layer. During extrusion, several bead deposition parameters can be controlled such as the printing speed, extrusion speed, bead dimensions, and nozzle exit diameter. However, these parameters are not independent and play a strong role in determining the deformation mechanisms that the extrudate undergoes. A schematic of the extrudate is illustrated in Fig.1. At section A, fibers are mostly aligned with the flow due to the convergent zone in the nozzle. Shear flow at the walls of the nozzle can cause fibers to have higher alignment in the shell region with a less aligned core at the center of the nozzle. Hence, nozzle diameter plays a crucial role in determining the initial conditions of fiber orientation in the extrudate and the extent of this core-shell effect. Upon exiting the nozzle, the extrudate is sheared between the bottom surface of the nozzle and the moving substrate, and the extent of shearing depends on the gap between the nozzle and the substrate. This gap is equal to the layer height if no further compaction occurs. In current study, we use a tamper to compact the bead and hence the final bead height is equal to the difference of initial gap and tamping distance. The parameter bead aspect ratio is equal to the ratio of bead width and bead height, and determines the extent of squeezing of the bead. Bead height is equal to the distance between the exit surface of the nozzle and the substrate (without compactor). Another important parameter is the ratio of the extrusion speed to the printing speed which also translates to the ratio of the cross-section area of the bead to the cross-section area of the nozzle. A bead to nozzle area ratio of less than 1 indicates stretching of the extrudate as it is laid down, while a ratio greater than 1 indicates compression of the extrudate in front of the nozzle, thereby

causing lateral flow. As elongational flow helps in fiber alignment, this ratio affects the final fiber orientation of printed bead. Based on this understanding, three crucial deposition parameters are identified - nozzle size, bead aspect ratio and bead to nozzle area ratio.

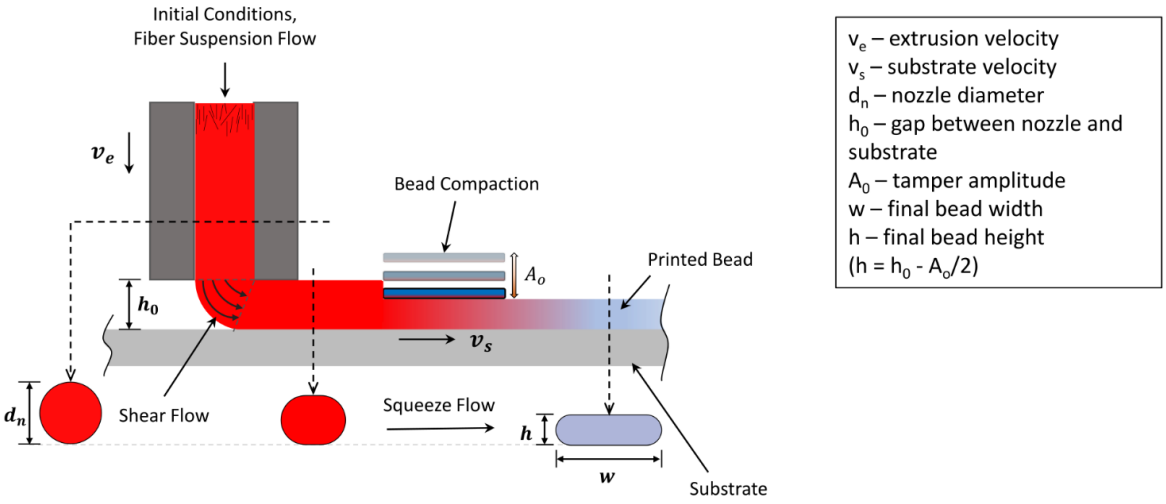

Figure 1: Schematic representation of deformation mechanisms developed during the bead deposition process.

Once the processing parameters of interest were chosen, we performed a design of experiments on these parameters to understand the effect of the bead deposition conditions on the tensile stiffness and strength. The first parameter to study is the bead to nozzle area ratio. We considered two values of bead to nozzle area ratio – 0.8, and 1.2. These condition capture cases where the printed bead is being stretched and compressed respectively. Note that these values indirectly give us information on the ratio between extrusion velocity and the nozzle velocity. The velocity ratio can be found using a simple volume conservation is given by the reciprocal of the bead to nozzle are ratio. The second parameter we varied is the bead aspect ratio. The bead aspect ratio is defined as the width to height ratio of the printed bead. We considered two values of bead aspect ratio: 2 and 6. These values are chosen to represent extreme cases of the general bead aspect ratio used during printing which is 4. Third, and finally, we considered three nozzle sizes for the experiments, 3 mm, 4 mm, and 5 mm. The design of experiments is summarized in Table 1.

Table 1: Printing conditions used for the experiments.

Nozzle diameter, d_n (mm)	**3 mm**			
Bead to nozzle area ratio (A_b/A_n)	0.8		1.2	
Bead aspect ratio, BAR (w/h)	2	6	2	6
Nozzle area, A_n (mm^2)	7.069	7.069	7.069	7.069
Bead area, A_b (mm^2)	5.655	5.655	8.482	8.482
Bead height, h (mm)	1.780	0.989	2.180	1.211
Bead width, w (mm)	3.559	5.932	4.359	7.265
Nozzle diameter, d_n (mm)	**4 mm**			
Bead to nozzle area ratio (A_b/A_n)	0.8		1.2	
Bead aspect ratio, BAR (w/h)	2	6	2	6
Nozzle area, A_n (mm^2)	12.566	12.566	12.566	12.566
Bead area, A_b (mm^2)	10.053	10.053	15.080	15.080
Bead height, h (mm)	2.373	1.318	2.906	1.614
Bead width, w (mm)	4.746	7.909	5.812	9.687
Nozzle diameter, d_n (mm)	**5 mm**			
Bead to nozzle area ratio (A_b/A_n)	0.8		1.2	

Bead aspect ratio, BAR (w/h)	2	6	2	6
Nozzle area, A_n (mm^2)	19.635	19.635	19.635	19.635
Bead area, A_b (mm^2)	15.708	15.708	23.562	23.562
Bead height, h (mm)	2.966	1.648	**3.633**	2.018
Bead width, w (mm)	5.932	9.887	7.266	**12.108**

Having discussed the conditions to be examined, we now discuss the experimental methods to prepare tensile coupons. We evaluate the effect of the processing conditions on the elastic stiffness in the printing direction and stacking direction. These tensile tests not only serve in understanding the effect of processing conditions on the tensile stiffness, but also serve as inputs to infer the fiber orientation state in the printed bead. This step will be discussed in the next section. We use the Composites Additive Manufacturing Research Instrument (CAMRI) to print specimens to be tensile tested. CAMRI is a medium scale extrusion deposition system developed at Purdue University to investigate the phenomenon governing the manufacturing process in EDAM. Details about of the system can be found elsewhere [18]. In the discussions that follow, we refer to the printing direction as 1-direction, the direction transverse to the printing direction in the same plane as 2-direction, as the stacking direction as 3-direction. For each printing condition listed in Table 1, one bead thick rectangular walls with dimensions of 0.28 m (1-direction) × 0.05 (2-direction) m × 0.25 (3-direction) m are printed. The panels are heat treated at 180 C for two hours after which specimens to be tensile tested are sectioned using a water-jet. The samples are heat treated to alleviate residual stresses arising due manufacturing process. An illustration of the printed panels and how specimens are extracted to prepare tensile coupons in the 1-direction and 3 – direction are shown in Fig. 2 and Fig. 3 respectively.

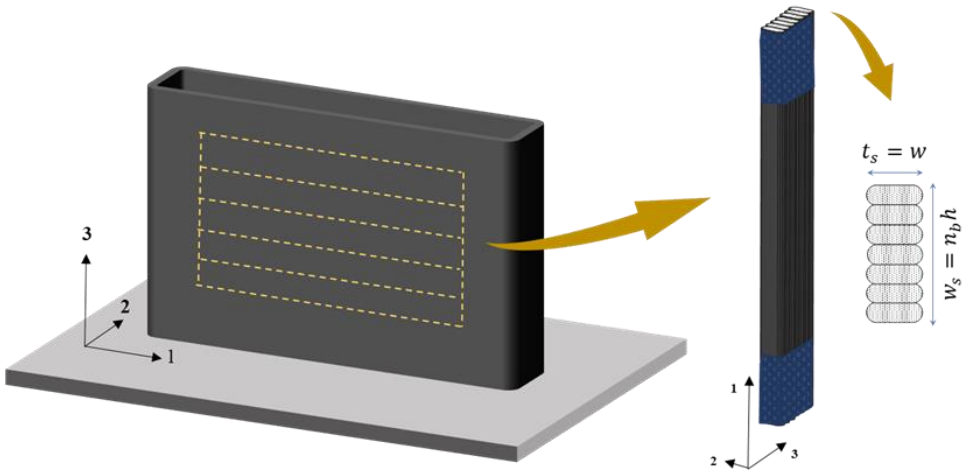

Figure 2: Tensile coupon (not shown to scale) with emery cloth (illustrated in blue) attached to the top and bottom of the samples. Dimensions of bead illustrated in terms of the bead width and bead height.

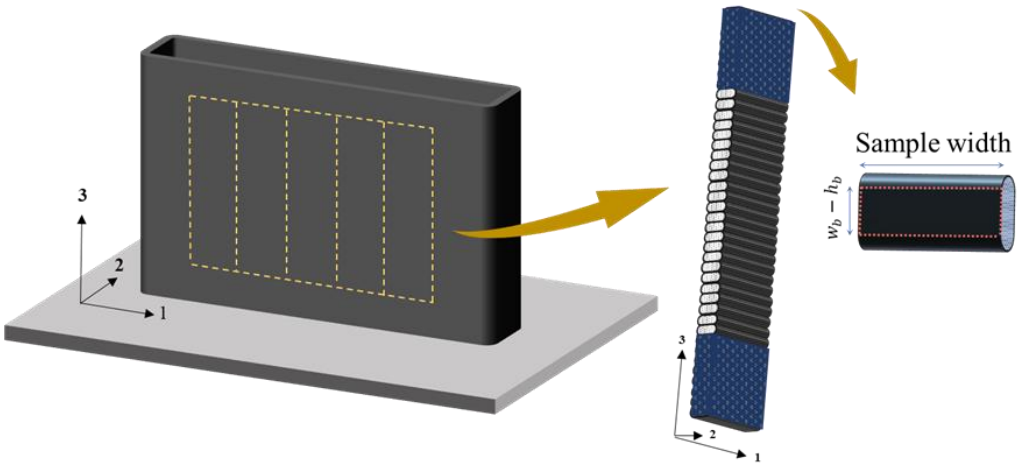

Figure 3: Tensile coupon (not shown to scale) with emery cloth (illustrated in blue) attached to the top and bottom of the sample. The cross-sectional area (dashed red border) approximated as the product of sample width and length of contact area (bead width – bead height).

For the 1-direction specimens, the tensile coupons are made 17.8 mm wide, 228.6 mm long, and with 38.1 mm long tabs on each end, thus resulting in an effective gage length of around 152 mm. The thickness of each tensile coupon was equal to the corresponding bead width. A speckle pattern is applied on the surface of the coupons for characterizing the strains field developed throughout the test via Digital Image Correlation (DIC) (Correlated Solutions Inc, Irmo, SC. USA). Tensile tests are carried out in a 22-kip MTS load frame at a loading rate of 2 mm/min and with DIC image acquisition interval of 200 milliseconds. To prevent the samples from slipping, emery cloth was applied on both ends of the sample to enhance load transfer from the grips. For stress calculations, the cross section is taken as a rectangle with semi-circle edges (stadium shape) and summed over the number of beads, as shown in Fig. 2.

For the 3-direction specimens, the tensile coupons are made 25.4 mm wide, 177.8 mm long, and with 31.7 mm long tabs on each end, thus resulting in an effective gage length of around 114 mm. The thickness of each tensile coupon was equal to the corresponding bead width. Similar to the 1-direction specimens, a speckle pattern is applied on the surface of the coupons for recording of strains fields via Digital Image Correlation (DIC) (Correlated Solutions Inc, Irmo, SC. USA). Since the surface of the specimens are not machined, applying a stochastic pattern using a roller is not possible. Instead, the specimens are first sprayed with white matte paint. Next, to emulate the stochastic black pattern to be tracked via the DIC, the specimen is carefully sprayed with a black paint from a distance to create a random distribution of trackable points. Tensile tests are carried out in a 22-kip MTS load frame at a loading rate of 1 mm/min and with DIC image acquisition interval of 100 milliseconds. To prevent the samples from slipping, emery cloth was applied on both ends of the sample to enhance load transfer from the grips. The cross-sectional area used for calculating stresses in 3-direction is corrected to resemble the true contact area between beads as opposed to the entire bead width times sample width, as shown in the red dotted box in Figure 3.

For each printing condition, five tensile coupons are prepared for the 1- and 3-direction specimens. We follow the ASTM D3039 standard to conduct the tensile tests. Note, that we do not machine the sample to a planar smooth surface. This ensures we capture the fiber orientation effect of the whole bead. The illustration of the tensile specimens in Fig. 2 and Fig. 3 show the bead surfaces.

Inference of Fiber Orientation

Once the tensile tests are conducted, we use this information to infer the fiber orientation state induced by two different processing conditions. First, we infer the orientation state corresponding to the processing parameters that lead to the highest elastic stiffness in the 1-direction (highest E_1 case) and second, we infer the orientation state corresponding to the processing conditions that lead to the lowest value of the elastic stiffness in the 1-direction (lowest E_1 case). It is expected that the highest stiffness in the 1-direction will be caused by a higher number of fibers aligned in the 1-direction and the lowest stiffness in the 1-direction will correspond to the case where the fibers are not preferentially aligned in the 1-direction. To characterize the fiber orientation state in the polymer, we use an inference framework from our previous work [19] wherein we infer the second order orientation tensor using tensile tests results. We provide a quick summary of the methodology below.

The framework utilizes three components. First, we use a micromechanics model to predict the elastic stiffness components of the composite, given the polymer elastic properties and the orientation tensor. A two-step homogenization method [20] which utilizes the Mori-Tanaka model is used in this work [21]. The second order orientation tensor, following Advani and Tucker [22] is used to describe the orientation distribution of the fibers. In this study, the fibers orientation is assumed to possess only the three diagonal terms in the principal directions. This representation has shown to produce acceptable results for composite stiffness predictions as shown in Ref. [23]. Second, we utilize the experimental measurements to infer the fiber orientation state and polymer properties by minimizing a loss function defined as:

$$\mathcal{L}(f(x), y) = \sum_i \left(\frac{f_i(x)}{y_i} - 1 \right)^2,$$

where $f_i(x)$ is the micromechanics model prediction of the corresponding experiment, y_i, and x is the fiber orientation state and the polymer properties. The other required inputs to the micromechanics model are taken from [24]. We use three experimental values in this inference framework, namely the average elastic stiffness in the 1- and 3-direction, and the average Poisson's ratio in the 1-3 plane. Third, this framework utilizes the inferred parameters to populate the entire elasticity tensor. To account for noise in experimental measurements and the possible use of an expensive micromechanics model, we use a support vector regression-based surrogate to replace the loss function. For implementation details readers are directed to [19]. In this study the material system remains the same and only the processing parameters are changed. Therefore, we keep use the inferred properties of PESU from [19], [25] and only infer the fiber orientation state for the various processing conditions.

Virtual Investigation of Spring-In Deformation

Following the inference of the fiber orientation state for the various bead deposition conditions, micromechanics methods [20], [21] are used to determine homogenized properties required to populate digital material cards. The properties of the constituents, namely fiber and polymeric matrix, are determined following the approach by Thomas et al. [19]. Table 2 summarizes the material properties and microstructural descriptions required to generate a digital material card and relevant ASTM standards used for experimental characterization. The reader is referred elsewhere [25] for details on the experimental characterization methods and experimental results.

Table 2: Summary of material properties and microstructural descriptors required for generating digital material cards.

Material Property	Relevant Standard
Glass Transition Temperature	ASTM D7028
Fiber Orientation Distribution	
Fiber Length Distribution	
Elastic Properties (9 components)	ASTM D3039 ASTM D5379

Coefficient of Thermal Expansion (3 directions)	ASTM E831
Thermoviscoelastic Behavior (9 Prony series)	ASTM D5023
Thermal Conductivity (3 directions)	ASTM E1461
Heat Capacity	ASTM E1269

Once the material properties have been identified, we have the material card to run manufacturing simulations. In this study we use a sequentially coupled thermo-mechanical analysis. An in-house code, called ADDITIVE3D is used to achieve this. The simulation code has been developed in ABAQUS and details are reported elsewhere[6], [8]. To evaluate the effect of processing conditions we choose a geometry of interest that promotes spring-in deformation. To promote spring in, curvatures are required. Radford and Rennick developed an expression for the spring in of angled brackets in [26]. They showed that larger the radius of curvature, lower the distortion via spring in. Motivated by this observation, we select a geometry as shown in Fig. 5. We refer to this geometry as the racetrack geometry. As illustrated in Fig 5, this geometry contains three semicircular regions that promote spring in deformation. It is important to note that while the elastic moduli are important for the performance of the printed part, the coefficient of thermal expansion (CTE) is more relevant to the residual stresses and shape change during and after the printing process. Further, spring-in deformation in curved geometries is strongly influenced by the differences in the CTE in the hoop (1-Direction) and radial (2-Direction) directions. Previous investigations have shown that the amount of spring-in deformation is strongly related to the difference in CTE between the two material directions. While larger differences in CTE result in larger spring-in deformations, similar CTEs do not result into spring-in deformation. However, other mechanisms can influence the spring-in deformation, including thermal stresses resulting from printing multiple beads (side-to-side) along a curved region. The deposition of multiple beads side-to-side affects the stress distribution developed in the hoop direction and thus the spring-in deformation in curved geometries. The analysis presented here focuses only on single bead geometry. Fig. 4 compares the elastic moduli and the CTE in the 1-, 2-, and 3-direction for the cases studied here, i.e., the print conditions corresponding that produce the lowest and the highest elastic stiffness in the 1-direction.

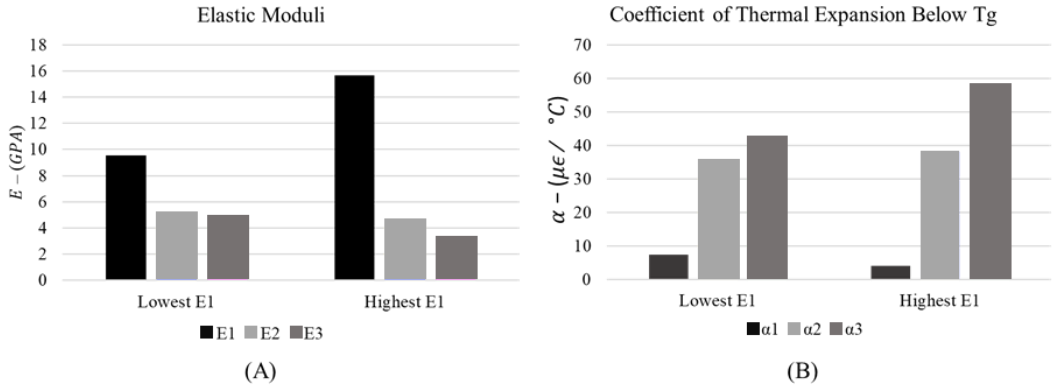

Figure 4: Comparison of elastic and thermomechanical properties for process conditions that yielded the highest and lowest E_1 . A) Comparison of elastic moduli. B) Comparison of CTE.

The dimensions of the geometry are shown in Fig. 5. We design for printing in the CAMRI system and thus the printed bead has dimensions corresponding to the physical print conditions. For the finite-element model, we discretize the bead with one element across the height and two elements across the width, thereby resulting in elements with average dimensions of 3.53 mm by 3.56 mm for the lowest E_1 case, and 1.71 mm by 1.81 mm for the highest E_1 case.

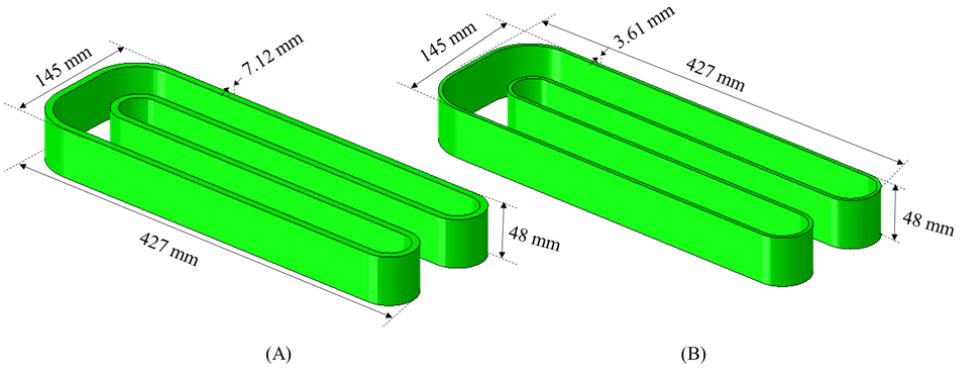

Figure 5: Dimensions of racetrack geometry used in virtual investigation. (A) Lowest E_1 case. (B) Highest E_1 case.

We simulate three steps in ADDITIVE3D, namely the printing process, cooling of the part while attached to the build plate (1 min), and cooling of the part to the room temperature after removal from the build plate. These steps are motivated by a real-world printing experiment and serves as the "digital twin" of the additive manufacturing process. For the simulations, we assume a perfectly bonded interaction of the part with the build substrate. Such an interaction is enforced using a kinematic boundary condition where all the degrees of freedom are constrained for the nodes on the bottom surface of the part. We make this assumption to remove the influence of the interaction of the part with the build plate on the residual deformation, however, models have been implemented to capture interactions with build sheets (thin polymer sheets), layers of adhesive, and bead boards [27]. We constrain a set of three nodes at the middle of the back wall to prevent rigid body motion when the part is taken off the print bed. The parameters used in the simulations are summarized in Table 3.

Table 3: Summary of the simulation parameters

Parameter	Value	
General Simulation Parameter	Lowest E_1 case	Highest E_1 case
Print speed	2500 mm/min	
Layer time	42.45 s	42.67 s
Elements per bead in the width direction	2	
Elements per bead in the height direction	1	
Total elements	13664	54880
Time cool on bed	60 s	
Time cool off bed	300 s	
Time increment deposition	3 s	
Time increment cooling steps	5 s	
Heat Transfer Parameters		
Ambient temperature	25°C (298.15 K)	
Printing bed temperature	100°C (373.15 K)	
Material Extrusion Temperature	379°C (652.15 K)	
Emissivity	0.96	
Compaction system	Tamper	
Power removed by the compactor	8000 W	

Results and Discussion

We first present the results from the tensile tests. Table 4 lists the average strength, the average elastic modulus in the 1-direction, and the major Poisson's ratio characterized for the 12 conditions.

Table 4: Strength, Modulus, and Poisson's ratio values characterized from tensile tests in the 1-direction.

Nozzle diameter, d_n (mm)	**3 mm**			
Bead to nozzle area ratio (A_b/A_n)	0.8		1.2	
Bead aspect ratio, BAR (w/h)	2	6	2	6
Avg. Tensile Strength, X_1 (MPa)	140.07	144.54	98.09	124.45
Avg. Elastic Modulus, E_1 (GPa)	15.65	15.47	10.66	11.69
Avg. Poisson's ratio, $\boldsymbol{\upsilon_{13}}$	0.35	0.36	0.40	0.43
Nozzle diameter, d_n (mm)	**4 mm**			
Bead to nozzle area ratio (A_b/A_n)	0.8		1.2	
Bead aspect ratio, BAR (w/h)	2	6	2	6
Avg. Tensile Strength, X_1 (MPa)	101.96	116.09	99.65	114.60
Avg. Elastic Modulus, E_1 (GPa)	12.54	13.22	10.54	11.40
Avg. Poisson's ratio, $\boldsymbol{\upsilon_{13}}$	0.37	0.38	0.43	0.45
Nozzle diameter, d_n (mm)	**5 mm**			
Bead to nozzle area ratio (A_b/A_n)	0.8		1.2	
Bead aspect ratio, BAR (w/h)	2	6	2	6
Avg. Tensile Strength, X_1 (MPa)	109.56	113.73	92.45	109.81
Avg. Elastic Modulus, E_1 (GPa)	12.39	13.24	9.53	10.32
Avg. Poisson's ratio, $\boldsymbol{\upsilon_{13}}$	0.40	0.43	0.42	0.46

The average elastic moduli in the 1-direction are compared in Fig. 6; different markers, background colors, and patterns are used to represent the bead aspect ratio, bead-to-nozzle area ratio, and nozzle size, respectively. The average elastic modulus in the 1-direction ranged between 9.53 GPa and 15.65 GPa whereas the average tensile strength ranged between 92.45 MPa and 144.54 MPa across the different printing conditions. The major Poisson's ratio ranged between 0.35 and 0.45. Increasing the bead aspect ratio from 2 to 6 increased the elastic modulus in the 1-direction. Such an increase can be observed in Fig. 6 by the points denoted by the rectangular and triangular markers across the blue and orange tiles. While it is expected that additional compaction will re-orient the fibers in the 2 direction, further studies are required to clarify the flow mechanism involved. The bead to nozzle area ratio produced the most significant change in E_1 for the three nozzle dimensions. As the bead to nozzle area ratio is reduced from 1.2 to 0.8, the deformation mechanisms in the extrudate transitions from squeeze flow in front of the nozzle to extensional flow in the bead. The latter flow mechanism increases the alignment of fibers in the printing direction, thereby increasing the elastic modulus in the 1-direction. Finally, reducing the nozzle size only resulted in a slight increase in the elastic modulus in the 1-direction.

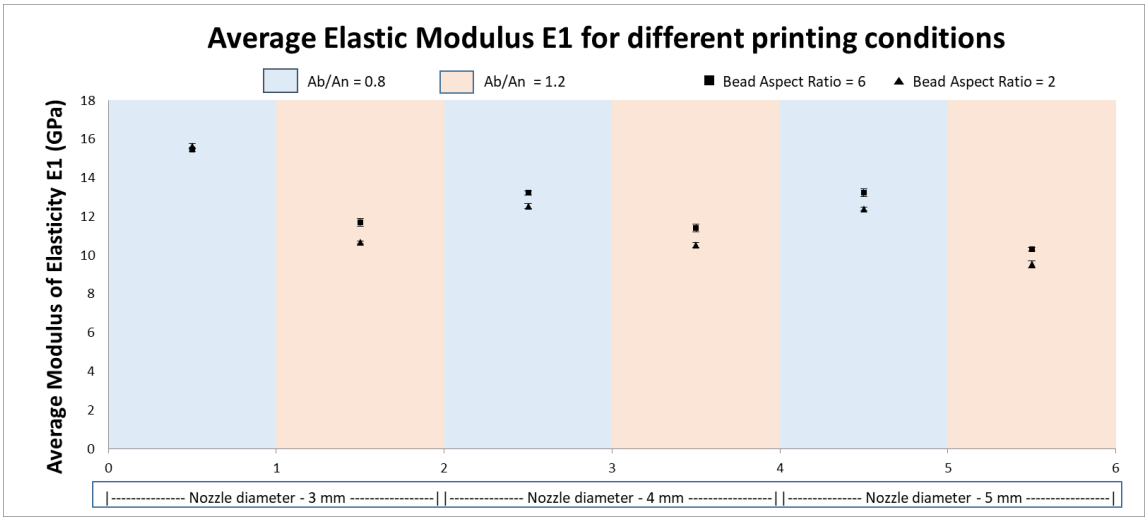

Figure 6: Comparison of the elastic modulus E1 (GPa) for different printing conditions.

Next, we discuss the results from the tensile tests in the 3-direction. Table 5 lists the average strength, the average elastic modulus in the 1-direction, and the minor Poisson's ratio characterized for the 12 conditions.

Table *5*: Strength, Modulus, and Poisson's ratio values characterized from tensile tests in the 3-direction.

Nozzle diameter, d_n (mm)	**3 mm**			
Bead to nozzle area ratio (A_b/A_n)	0.8		1.2	
Bead aspect ratio, BAR (w/h)	2	6	2	6
Avg. Tensile Strength, X_3 (MPa)	29.69	37.87	34.84	58.21
Avg. Elastic Modulus, E_3 (GPa)	3.35	4.28	4.50	4.81
Avg. Poisson's ratio, $\boldsymbol{\upsilon_{31}}$	0.07	0.08	0.11	0.14
Nozzle diameter, d_n (mm)	**4 mm**			
Bead to nozzle area ratio (A_b/A_n)	0.8		1.2	
Bead aspect ratio, BAR (w/h)	2	6	2	6
Avg. Tensile Strength, X_3 (MPa)	25.03	36.49	16.45	33.56
Avg. Elastic Modulus, E_3 (GPa)	3.76	3.80	4.83	4.70
Avg. Poisson's ratio, $\boldsymbol{\upsilon_{31}}$	0.07	0.10	0.13	0.15
Nozzle diameter, d_n (mm)	**5 mm**			
Bead to nozzle area ratio (A_b/A_n)	0.8		1.2	
Bead aspect ratio, BAR (w/h)	2	6	2	6
Avg. Tensile Strength, X_3 (MPa)	33.88	23.42	24.06	36.22
Avg. Elastic Modulus, E_3 (GPa)	4.34	4.33	4.89	4.16
Avg. Poisson's ratio, $\boldsymbol{\upsilon_{31}}$	0.08	0.11	0.13	0.15

The average elastic modulus in the 3-direction is compared in Fig. 7; different markers, background colors, and patterns are used to represent the bead aspect ratio, bead-to-nozzle area ratio, and nozzle size, respectively. The average elastic modulus in the 3-direction ranged from 3.35 GPa to 4.89 GPa whereas the average tensile strength ranged from 16.45 MPa to 58.21 MPa. The minor Poisson's ratio ranged between 0.07 and 0.15. Similar to the results in the 1-direction, increasing the bead aspect ratio from 2 to 6 increased the elastic modulus in the 3-direction for most of the cases, which can be explained by the increase in contact area between beads resulting from a larger aspect ratio. Furthermore, we observer that increasing the bead to nozzle area ratio also increased the elastic modulus, which can be explained by the dominance of squeeze flow at bead to nozzle area ratios greater than one and the corresponding effect of re-aligning the fibers from the printing direction to other directions.

Thus, the orientation of fibers in the 3-direction increases relative to the condition with a bead to nozzle area ratio less than one. Similar to the results in the 1-direction, we observe that changing the nozzle size did not significantly affect the elastic modulus in the 3-direction.

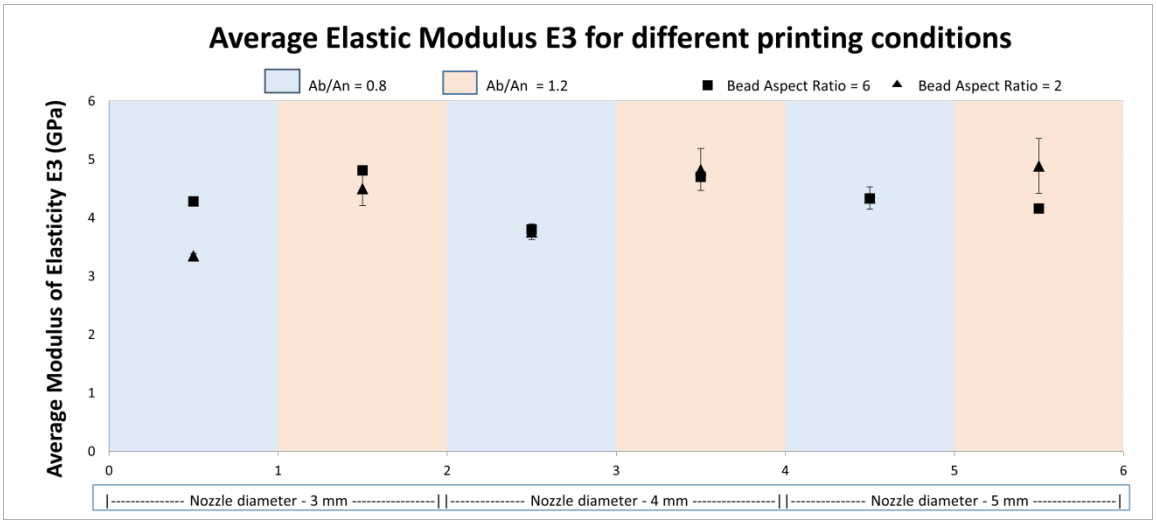

Figure 7: Comparison of the elastic modulus E3 (GPa) for different printing conditions.

Next, as discussed in the earlier section, we use the tensile test information to infer the fiber orientation state using the inference methodology. The diagonal components of the inferred orientation state for the highest and lowest case are listed in Table 6 and Table 7 respectively. The results agree with intuition. A higher stiffness in the 1-direction would be caused by the higher alignment of fiber in this direction. Similarly, a lower value of stiffness in the 1-direction would be caused by lower alignment of fibers in the 1-direction. Table 6 shows that the term a_{11} has a value of 0.77 indicating higher fiber alignment. Table 7 shows that the term a_{11} has a only value of 0.60 (much lower than 0.77 in the case of the highest E_1)indicating lower fiber alignment in the 1-direction and consequently the lowest stiffness.

Table 6: Orientation tensor inferred for the process condition that yielded the highest E_1.

Diagonal entries of Fiber Orientation Tensor A_{ij}	Value
a_{11}	0.77
a_{22}	0.16
a_{33}	0.07

Table 7: Orientation tensor inferred for the process condition that yielded the lowest E_1.

Diagonal entries of Fiber Orientation Tensor A_{ij}	Value
a_{11}	0.60
a_{22}	0.22
a_{33}	0.18

After we populate the material cards using the inferred orientation, we perform the simulations as outlined in the earlier section. We first compare the stress profile developed in the two cases studied. Fig. 8 illustrates the stress profile developed in the 1-direction (print direction) during the printing process. The left column of Fig. 8 corresponds to the printing conditions that led to the lowest E_1, and the right column of Fig. 8 corresponds to the printing conditions that led to the highest E_1. A transition from compressive to tensile stresses develops from the convex side to the concave side in the curved regions of the racetrack, respectively. This stress distribution is the consequence of the self-constrained condition developed in curved regions where there is a CTE mismatch between the radial (2-direction) and hoop (1-direction) directions. Although stresses develop in both the hoop and radial directions, the distribution of hoop stresses is the primary cause of spring-in deformation.

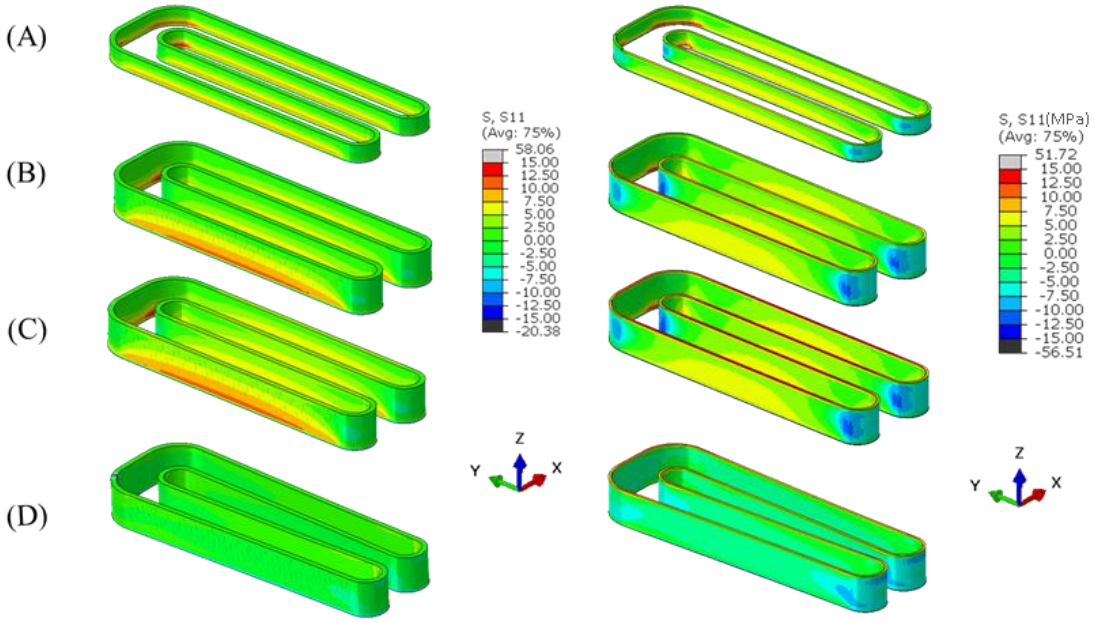

Figure 8: Stress distribution in the 1-direction (print direction) at different stages of the printing process. (A) Mid-way through deposition. (B) End of deposition. (C) After cooling on bed. (D) After cooling to ambient temperature. Left: lowest E_1 case. Right: highest E_1 case

The cross-section view of the racetrack in Figure 9 shows tensile stresses (1-Direction) developed on the concave side of a curved section of the racetrack for both deposition conditions. The racetrack with the largest difference in compressive to tensile stresses across the bead width also corresponds to the process conditions that yielded the largest difference in CTEs (highest E_1).

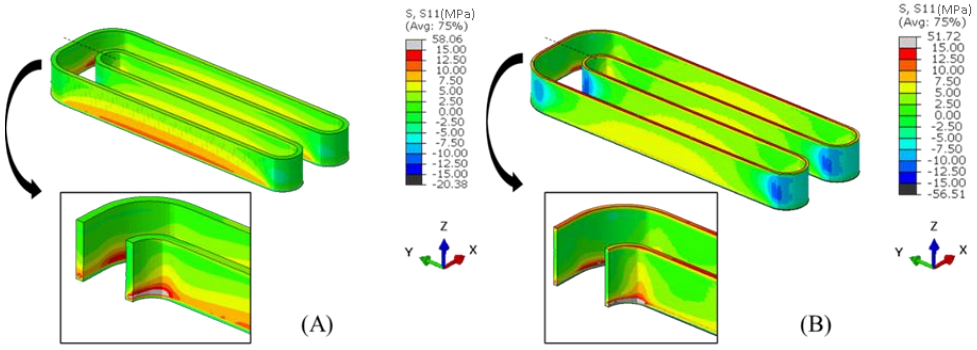

Figure 9: Stress distribution in the 1-direction (hoop direction) after cooling on bed with cross-section view at center of the geometry in the ZX plane (A) lowest E_1 case (B) highest E_1 case.

The removal of the part from the print bed results in spring in deformation. We compare the amount of spring-in deformation developed in the racetrack geometry with conditions that yielded the lowest E_1 and highest E_1. As shown in Fig. 10 both legs of the geometry deform towards the center of the racetrack (inwards). It should be noted the displacement shown in Fig. 8 is in the global coordinate system and corresponds to displacement in the X-direction. The spring-in deformation is characterized using the distance between the two legs at the open end of the racetrack as shown in Fig. 10 (A). Table 8 lists the distance between the two legs, the deformation calculated from the difference between the initial and final distances, and the deformation percentage. As expected, we observe that the largest deformation is developed with the process condition that yield the highest stiffness in the printing direction. A higher E_1 involves higher fiber alignment in the print direction but also a larger mismatch in CTE between the 1- and 2- directions. We observe from Table 8 that the magnitude of difference in deformation is not substantial. This is due to the fact that the difference in CTE between the two printing conditions is not substantially different. This virtual investigation gives us valuable insight into the causes of deformation in the EDAM process. As demonstrated, we studied cases where the stiffness variation is large but the resulting deformation is comparable due to the similarities in the CTE values. Although the difference in spring-in deformation is not substantial between the two process conditions, the difference in elastic modulus is more pronounced and would have a stronger impact in the performance of the printed material.

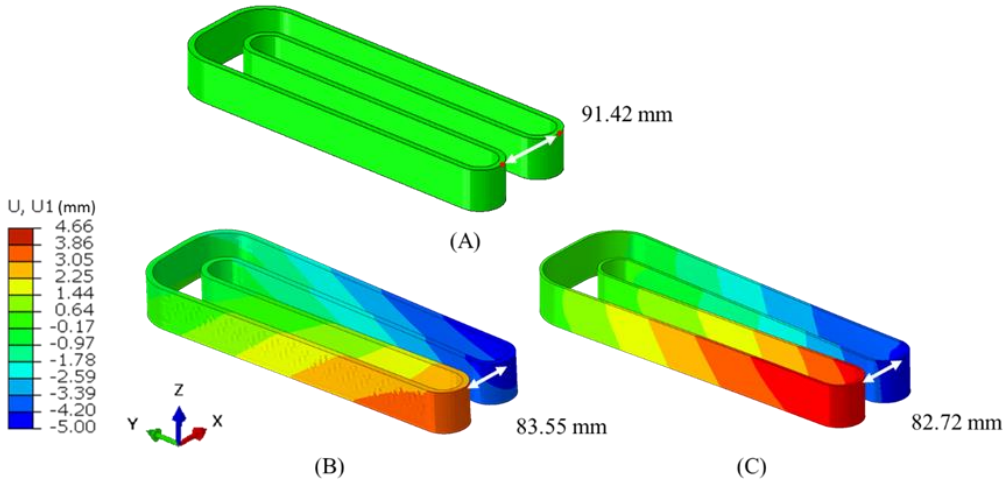

Figure 10: Spring-in deformation developed in the racetrack geometry. (A) Undeformed mesh. (B) Lowest E_1 case. (C) Highest E_1 case. Deformation shown with scale factor of 2.5.

Table 8:Deformed distance, deformation, and deformation (%) measured for the two material models.

	Distance between legs after Deformation(originally 91.42mm)	**Deformation (mm)**	**Deformation (%)**
Lowest E_1	83.55	7.87	8.61
Highest E_1	82.72	8.70	9.52

Conclusion

We conducted this preliminary investigation to understand the effect flow induced microstructure has on the residual deformation of a part printed via the extrusion deposition additive manufacturing process. We started by understanding the effect of the nozzle diameter, bead to nozzle aspect ratio, and bead aspect ratio has on the elastic properties in the printing and stacking direction. The experimental results showed the bead to nozzle area

ratio to have the strongest influence on the elastic moduli of the printed material. It was also observed that the nozzle dimeter had minimal effects on the elastic modulus. However, after cleaning the nozzle and measuring the diameter it was observed that the 4 mm nozzle had a diameter of 4.5 mm. Therefore, the results presented for the 4mm and 5 mm nozzle only vary by a small amount. Next, to understand the effect of the bead deposition conditions we chose two processing conditions to evaluate. These processing conditions corresponded to the cases which resulted in the highest and lowest stiffness in the printing direction. To enable the manufacturing simulations, we infer the fiber orientation state using an inference methodology coupled with a micromechanics model. Using this microstructural information corresponding to the printing conditions we populate the material card needed to run the manufacturing simulations. We chose to virtually print a geometry that is prone to spring-in deformation. The results of this virtual investigation showed less spring-in deformation in the part printed with the deposition conditions that yielded the lowest stiffness in the printing direction compared to the part printed with deposition conditions that yielded the highest stiffness in the printing direction. Although a significant difference in the elastic modulus was observed between these two conditions, the difference in coefficient of thermal expansion between the 1 and 2 directions was not substantial. Therefore, the observed change in deformation between the two extreme cases was not as substantial as the change in elastic modulus.

This study serves as an initial investigation on the effect of bead deposition conditions and we suggest futures avenues of research. First, the predicted spring-in deformation should be experimentally validated. Further, this study focused on the spring in deformation of a racetrack geometry. Other geometries of interest include a flat plate with anti-symmetric print orientation. Example of an anti-symmetric orientation include a four-layer print geometry with the print orientation of the first two layers perpendicular to the last two layers. This geometry is prone to out-of-plane deformation and is potentially a good candidate for investigation. Finally, a direction of future research could be the consideration of uncertainty in fiber orientation. Following [28], we can use a distribution of orientation tensors to enable probabilistic predictions of spring-in or warpage in additive manufacturing simulations.

Acknowledgements

This research was sponsored by Lockheed Martin Corporation

References

[1] A. A. Hassen *et al.*, “Scaling Up Metal Additive Manufacturing Process to Fabricate Molds for Composite Manufacturing,” *Additive Manufacturing*, vol. 32, no. March 2019, p. 101093, 2020, doi: 10.1016/J.ADDMA.2020.101093.

[2] L. J. Love *et al.*, “The importance of carbon fiber to polymer additive manufacturing,” *Journal of Materials Research*, vol. 29, no. 17, pp. 1893–1898, 2014, doi: 10.1557/jmr.2014.212.

[3] E. Barocio, B. Brenken, A. Favaloro, and R. B. Pipes, “Extrusion deposition additive manufacturing of composite molds for high-temperature applications,” 2017.

[4] G. Kim, E. Barocio, and R. Sterkenburg, “Enhancing Part Demolding Characteristics of Additively Manufactured Fiber-Reinforced Polymer Composite Tools via Surface Coating,” *Additive Manufacturing*, p. 102072, 2021.

[5] M. Bogdanor *et al.*, “Design of Composite Compression Molding Tools Using Large Scale Additive Manufacturing,” 2020.

[6] B. Brenken, E. Barocio, A. Favaloro, V. Kunc, and R. B. Pipes, “Development and validation of extrusion deposition additive manufacturing process simulations,” *Additive Manufacturing*, vol. 25, 2019, doi: 10.1016/j.addma.2018.10.041.

[7] M. R. Talagani *et al.*, “Numerical simulation of big area additive manufacturing (3D printing) of a full size car,” *SAMPE Journal*, vol. 51, no. 4, pp. 27–36, 2015.

[8] E. Barocio, B. Brenken, A. Favaloro, M. Bogdanor, and R. B. Pipes, “Extrusion Deposition Additive Manufacturing with Fiber-Reinforced Thermoplastic Polymers,” in *Structure and Properties of Additive Manufactured Polymer Components*, 1st ed., K. Friedrich and R. Walter, Eds. Woodhead Publishing,

2020, p. 450. [Online]. Available: https://www.elsevier.com/books/structure-and-properties-of-additive-manufactured-polymer-components/friedrich/978-0-12-819535-2
[9] C. Camposeco-Negrete, P. Y. Lavertu, and J. Lopez-de-Alda, "Prediction and optimization of the yield stress of material extrusion specimens made of ABS, using numerical simulation and experimental tests," *International Journal of Advanced Manufacturing Technology*, vol. 118, no. 11–12, pp. 3657–3671, Feb. 2022, doi: 10.1007/S00170-021-08180-2.
[10] P. Obst, M. Launhardt, D. Drummer, P. V. Osswald, and T. A. Osswald, "Failure criterion for PA12 SLS additive manufactured parts," *Additive Manufacturing*, vol. 21, pp. 619–627, May 2018, doi: 10.1016/J.ADDMA.2018.04.008.
[11] Y. Zhao, Y. Chen, Y. Z.-M. & Design, and undefined 2019, "Novel mechanical models of tensile strength and elastic property of FDM AM PLA materials: Experimental and theoretical analyses," *Elsevier*.
[12] J. Yan, E. Demirci, A. Ganesan, and A. Gleadall, "Extrusion Width Critically Affects Fibre Orientation in Short Fibre Reinforced Material Extrusion Additive Manufacturing," *Additive Manufacturing*, p. 102496, 2021, doi: 10.1016/j.addma.2021.102496.
[13] P. Pibulchinda, E. Barocio, and R. B. Pipes, "Influence of Fiber Orientation on Deformation of Additive Manufactured Composites," *Additive Manufacturing*, no. November, p. 102483, 2021, doi: 10.1016/j.addma.2021.102483.
[14] A. Tezvergil, L. V. J. Lassila, and P. K. Vallittu, "The effect of fiber orientation on the thermal expansion coefficients of fiber-reinforced composites," *Dental Materials*, vol. 19, no. 6, pp. 471–477, Sep. 2003, doi: 10.1016/S0109-5641(02)00092-1.
[15] W. Ogierman, G. K.-A. Mechanica, and undefined 2016, "A study on fiber orientation influence on the mechanical response of a short fiber composite structure," *Springer*, vol. 227, no. 1, pp. 173–183, Jan. 2016, doi: 10.1007/s00707-015-1417-0.
[16] S. Mortazavian, A. F.-C. part B. engineering, and undefined 2015, "Effects of fiber orientation and anisotropy on tensile strength and elastic modulus of short fiber reinforced polymer composites," *Elsevier*.
[17] J. Ko and J. R. Youn, "Prediction of fiber orientation in the thickness plane during flow molding of short fiber composites," *Polym Compos*, vol. 16, no. 2, pp. 114–124, 1995.
[18] E. Barocio, "Fusion Bonding of Fiber Reinforced Semi-Crystalline Polymers in Extrusion Deposition Additive Manufacturing," Ph.D. Dissertation - Purdue University, 2018.
[19] A. J. Thomas, E. Barocio, and R. B. Pipes, "A machine learning approach to determine the elastic properties of printed fiber-reinforced polymers," *Composites Science and Technology*, vol. 220, p. 109293, Mar. 2022, doi: 10.1016/J.COMPSCITECH.2022.109293.
[20] I. Doghri and L. Tinel, "Micromechanical modeling and computation of elasto-plastic materials reinforced with distributed-orientation fibers," *International Journal of Plasticity*, vol. 21, no. 10, pp. 1919–1940, Oct. 2005, doi: 10.1016/J.IJPLAS.2004.09.003.
[21] T. Mori and K. Tanaka, "Average stress in matrix and average elastic energy of materials with misfitting inclusions," *Acta Metallurgica*, vol. 21, no. 5, pp. 571–574, May 1973, doi: 10.1016/0001-6160(73)90064-3.
[22] S. Advani, C. T. I.-J. of rheology, and undefined 1987, "The use of tensors to describe and predict fiber orientation in short fiber composites," *sor.scitation.org*, vol. 31, no. 8, p. 751, Nov. 1987, doi: 10.1122/1.549945.
[23] D. Dray, P. Gilormini, G. R.-C. S. and Technology, and undefined 2007, "Comparison of several closure approximations for evaluating the thermoelastic properties of an injection molded short-fiber composite," *Elsevier*.
[24] M. A. Ramirez and A. Dissertation, "Computational Viscoelastic Damage Modeling of Composite Materials in Extrusion Deposition Additive Manufacturing," 2021.
[25] E. Barocio, V. Kapre, P. Pibulchinda, M. A. Ramirez, A. Franc, and J. Susnjara, "Material Characterization for Large Scale Additive Manufacturing (AM)," U.S. DEPARTMENT OF ENERGY, Institute for Advanced Composites Manufacturing Innovation. Knoxville, TN. USA, 2022. [Online].

Available: https://iacmi.org/wp-content/uploads/2022/05/IACMI-7.6-Final-Project-Report-5-5-22-APPROVED.pdf
[26] D. W. Radford and R. J. Diefendorf, “Shape Instabilities in Composites Resulting from Laminate Anisotropy,” *Journal of Reinforced Plastics and Composites*, vol. 12, no. 1, pp. 58–75, 1993, doi: 10.1177/073168449301200104.
[27] E. Barocio, A. J. Thomas, and R. B. Pipes, “Virtual Investigation of Residual Part Deformation Due to Build Plate Support Characteristics in Material Extrusion Additive Manufacturing,” 2020.
[28] A. J. Thomas, E. Barocio, I. Bilionis, and R. B. Pipes, “Bayesian Inference of Fiber Orientation and Polymer Properties in Short Fiber-Reinforced Polymer Composites,” Feb. 2022.